# Aqueous Synthesis of Copper(II)-Imidazolate Nanoparticles

María F. Navarro Poupard[1], Ester Polo[1], Pablo Taboada[2], Ana Arenas-Vivo[3], Patricia Horcajada*[3], Beatriz Pelaz*[1] and Pablo del Pino*[1]

[1] Centro Singular de Investigación en Química Biolóxica e Materiais Moleculares (CiQUS), Departamento de Física de Partículas, Universidade de Santiago de Compostela, 15782 Santiago de Compostela (Spain)

[2] Departamento de Física de Partículas, Universidade de Santiago de Compostela, 15782 Santiago de Compostela (Spain)

[3] Advanced Porous Materials Unit, IMDEA Energy, 28935 Móstoles-Madrid (Spain);

* Correspondence to: patricia.horcajada@imdea.org, beatriz.pelaz@usc.es and pablo.delpino@usc.es

**Abstract:** A green, simple and efficient room temperature aqueous synthetic route for the fabrication of novel porous coordination polymer nanoparticles (NPs) composed of $Cu^{2+}$ and imidazolate was developed. Colloidal stability, morphology changes and structural and chemical integrity of the developed NPs, in several solvents having different polarity, were investigated. Basics physicochemical properties of selected NPs (*i.e.*, NP1, NP2 and NP3), such as size, optical and magnetic activity, porosity, thermal stability, structure, ageing and catalytic activity, were determined. Data indicate that the addition of the surfactant hexadecyltrimethylammonium bromide (CTAB) and the final solvent determine the size, morphology and structure of the different NPs.

**Keywords:** porous coordination polymers (PCPs), copper, nanoparticle, nanoscale PCP, physicochemical properties, catalysts

**INTRODUCTION**

Coordination polymers (CPs) are one-, two-, or three dimensional (1D, 2D, or 3D) polymeric compounds formed by repeating coordination entities (*i.e.*, inorganic, organic or hybrids inorganic-organic). There are several subclasses of CPs, including amorphous CPs, porous coordination polymers (PCPs), metal organic materials (MOMs), metal-organic frameworks (MOFs), coordination networks (CNs), and so forth. Definitions (nomenclature) in this supramolecular chemistry area seem to have become entangled with the arrival of the term MOF, which has revolutionized this field and its applications. Here, we adopt the following definition of MOF: "a class of CPs comprising organic linkers wherein metal−ligand interaction/bonding leads to 2D or 3D crystalline network structures" as proposed by S. Seth and A. J. Matzger.[1] The initial research interest of PCPs was mainly driven by their structure-dependent network of voids, which makes them ideal materials for storage and separation of different molecules and macromolecules, and for catalysis. PCPs are formed by cation centers, or clusters, interconnected by polydentate organic ligands through strong ionocovalent bonds,[2-4] and may be highly porous, having very low density (in the range of 0.2 $g \cdot cm^{-3}$). Recently, nonporous high-density MOFs have been proposed as next generation functional materials in diverse fields.[5,6] The vast diversity of reported PCPs (over 20,000 structures) in terms of crystal size, porosity, geometry and functionality is due to the multiple possible combinations of metallic centers and organic ligands.[7,8] Since the late 1990s, CP chemistry and related applications have greatly evolved from the pioneering contributions on reticular synthesis involving metal centers and organic linkers,[9] mostly by the groups of O. M. Yagui,[10,11] G. Férey,[12] R. Robson,[13] and S. Kitakawa.[14]

Initial efforts on PCP chemistry were put on building crystalline new porous bulk three-dimensional structures, in which synthetic control over crystal size, shape and dispersity was not the key objective. This was so because large single crystals usually facilitate the faster structural resolution of new crystalline phases, as well as because pore size and physicochemical stability were the most useful characteristics in applications such as storage and catalysis. Besides this conventional research aim, recent efforts are also focused on the precise control and modulation of the crystal size and shape and their integration in applicable devices.

In contrast to pure inorganic materials, in which the nanoscale dimension brings new, highly useful, physicochemical properties (*e.g.*, nanomagnetism, nanoplasmonics, quantum-dots), PCPs, independently of their size, porosity or structure, exhibit localized electronic states rather than delocalized ones.[15] As a result, nanoscale PCPs (*i.*e. nanoPCPs) offer a large surface area and ordered tunable porosity that is of great interest for relevant applications such as drug-delivery and device-material nanotechnology.[16-18] Composite nanomaterials composed of nanoPCPs and inorganic NPs have been proposed to produce multifunctional nanomaterials (*e.g.*, surface enhanced Raman scattering nanoprobes,[19] therapeutics,[20] theranostic agents[21,22]) for bioapplications and enhanced catalysis.[23,24] Notice that here amorphous or 1D nanoscale colloids made of organic ligands and metal centers (as in crystalline MOFs) will be referred to as nanoscale CPs (*i.e.*, nanoCPs),[25] whereas nanoPCPs will be here referred to as PCP crystals having all of their lateral dimensions within the size range of 1-500 nm, although any PCP may be considered nanostructured due to the network of nanometric voids.

Overall, rather few protocols exist to prepare monodisperse nanoPCPs compared with those to fabricate bulk PCPs; some exceptions are Zeolitic Imidazolate Framework 8 (ZIF-8),[19,26,27] diverse

MIL (MIL-53, MIL-88A, MIL-88Bt, MIL-89, MIL-100 and MIL-101_$NH_2$; MIL = Materials of Institut Lavoisier),[28,29] diverse UiO (UiO-66, UiO-66–$NH_2$, UiO-67, UiO-68–$NH_2$; UiO = Universiteteti Oslo),[30-32] M-TCPP (M = Zn, Cu, Cd or Co, TCPP = tetrakis(4-carboxyphenyl)porphyrin) nanosheets,[33] Prusian Blue,[34] HKUST-1 (HKUST = Hong Kong University of Science and Technology),[35,36] porphyrinic-Zr MOF,[37] NU-1000 (NU = Northwestern University),[38] and others (*cf*. recent review articles [16,39]).

To attain the fine control of both size and morphology of nanoPCPs, many chemical and microfabrication synthetic strategies have been proposed, including modified solvothermal routes (*e.g*. modulator agents, ligand modification), microwaves- and ultrasound-assisted methods, microemulsion, mechanochemistry or fluidics.[40] However, many of these approaches suffer from poor control of the particle size distribution and morphology, as well as low reaction yields. More recently, the use of surfactant under soft conditions (*i.e.*, water, low temperatures, atmospheric pressure) has revealed to be an asset compatible with large-scale production to control both the size and morphology of the zinc imidazolate ZIF-8.[41] With regards to $Cu^{+2}$-based nanoPCPs, and despite their industrial interest (*e.g.,* natural abundance, low cost, catalytic and conductive properties),[42] only few examples can be found in the literature, being mostly based on the HKUST-1 structure.[43-45] Within these works, the use of surfactants, such as hexadecyltrimethylammonium bromide (CTAB) or polyacrylic acid (PAA), has been also proposed as PCPs growth controlling additives [44,45]

Taking everything into account, the development of straightforward high-yield bottom-up methods to fabricate nanosized Cu-based nanoPCPs is desired to enhance their capabilities in catalytic applications. Herein, a straightforward aqueous synthetic route to produce highly monodisperse Cu-based nanoPCPs with different shape is described. Morphology and size of the crystallites, structure, colloidal stability, optical and magnetic activity, and catalytic properties of the NPs produced were investigated.

**RESULTS AND DISCUSSION**

Previous works have proposed a handful of chemical methods (bottom-up) for the fabrication of Cu-based CPs based on mixing $Cu^{+2}$ salts (mostly $Cu(NO_3)_2$) and organic ligands containing several carboxylates, such as 2,5-dihydroxyterephthalic acid,[46] 2-hydroxyterephthalic acid,[47] 3,3',5,5'- tetrakis(3,5-dicarboxyphenyl)-2,2',4,4',6,6'-hexamethylbiphenyl[48] and 1,3,5-benzenetricarboxylate.[49] Also, a few examples of Cu-based CPs built from imidazolates linker have been reported so far.[50-52]

Herein, NPs were fabricated by simply mixing aqueous solutions of $CuCl_2$ and 2-methylimidazole (2MI), which is the linker used together with $Zn^{2+}$ salts for the fabrication of the ZIF-8 solids.[53] As growth-arresting surfactant, CTAB was added using a molar ratio 2MI:CTAB of $10^3$, *cf.* Table 1 and Materials and Methods section. CTAB has been previously used to arrest ZIF-8 growing, thereby resulting in highly monodisperse ZIF-8 nanoMOFs and nanocomposites based on ZIF-8 and Au NPs.[19,54] In the present work, concentration and molar ratios of the reactants were optimized to produce monodisperse NPs (*i.e.*, sample Cu50 in Table 1), *cf*. Figure SI-I in the Supporting Information (SI). Sample Cu50 with molar ratio 2MI:$Cu^{2+}$ of 20 (and 2MI:CTAB of $10^3$) showed best monodispersity among all samples and thus, it is the focus of this work. Briefly, the aqueous solution containing copper, 2MI and CTAB was gently stirred for 1 min, in which the color of the solutions rapidly changed from bluish to brownish, *cf.* inset in Figure 1a. Our

hypothesis is that this change of color indicates the formation of the $Cu^{2+}$-imidazolate network, which growth is arrested by the presence of CTAB to yield monodisperse NPs. Then, the solution was left undisturbed for 45 min at room temperature (RT). The resulting compounds were then purified by centrifugation (7000 rcf, 15 min; unless otherwise specified, centrifugation parameters were fixed to these values), the colorless supernatant was discarded and the precipitate was redispersed and stored in 3 mL acetone. SEM inspection of the redispersed precipitate revealed the presence of NPs (in the following referred to as NP1), which show spherical morphology with an average diameter (d) of 330 ± 27 (0.5%) nm. The nanospheres NP1 (*i.e.*, Cu50 in Table 1) resembled an entangled network of nanosheets (thickness of less than 10 nm), *cf.* Figure 1a.

**Table 1.** $CuCl_2 \cdot 2H_2O$ concentrations and molar ratios used to produce different nanocomposites.

| **Sample**[1] | **$CuCl_2 \cdot 2H_2O$ [mM]** | **$Cu^{2+}$ : 2MI : CTAB [mol]** | **2MI:$Cu^{2+}$ [mol]** | **$Cu^{2+}$:CTAB [mol]** |
|---|---|---|---|---|
| Cu25 | 25 | 1 : 40 : 0.040 | 40 | 25 |
| Cu50 (NP1) | 50 | 1 : 20 : 0.020 | 20 | 50 |
| Cu67 | 67 | 1 : 15 : 0.015 | 15 | 67 |
| Cu100 | 100 | 1 : 10 : 0.010 | 10 | 100 |
| Cu200 | 200 | 1 : 5 : 0.020 | 5 | 200 |

[1] SEM images of all these samples can be found in the SI-1.

The influence of reaction time was investigated by letting the reaction progress at RT, undisturbed during 72 h (or longer; we checked up to 6 months with no significant visual colloidal stability differences, instead of 45 min employed for NP1). The brownish solution appearance remained similar (45 min *vs.* 72 h, or months) without the presence of apparent precipitates. After the 72 h, the nanocomposites were purified by centrifugation, the colorless supernatant was discarded and the precipitate was redispersed and stored in 3 mL acetone. SEM revealed the formation of thin nanosheets having an average edge length (L) of 334 ± 111 (33%) nm, *cf.* Figure 1b, which in the following will be referred to as NP2. We hypothesize that the thin entangled nanosheets of NP1 thermodynamically evolve to larger nanosheets (*i.e.*, NP2).

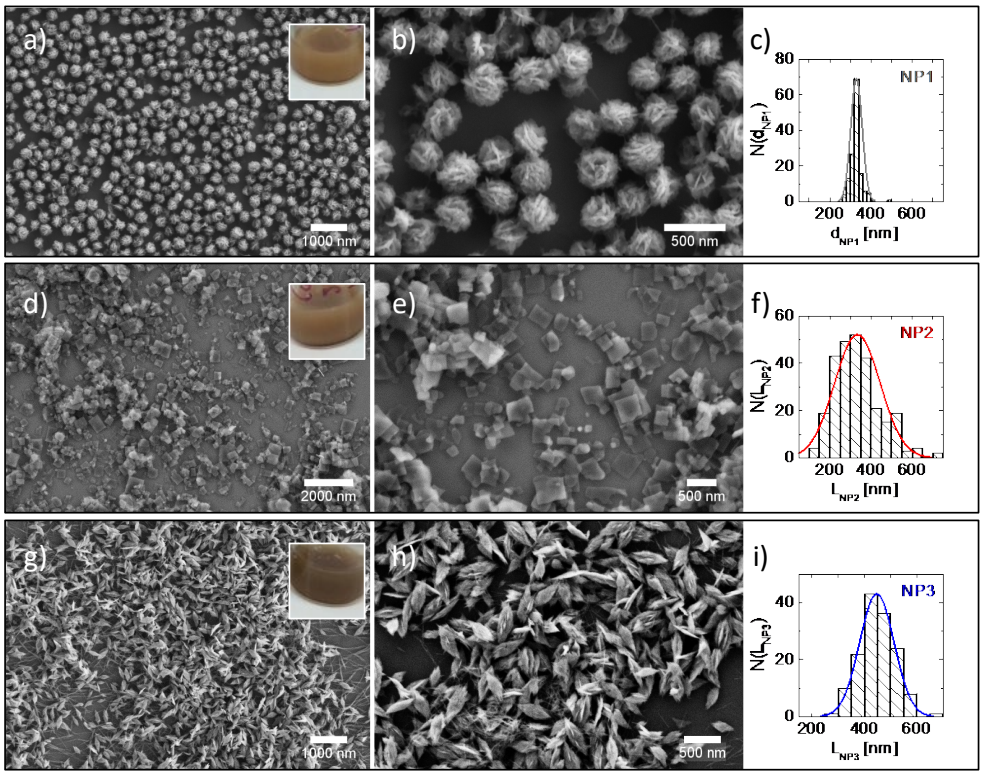


**Figure 1.** SEM micrographs of different species of Cu-imidazole nanocomposites after drop casting on Si substrates: a,b) NP1 with an average diameter of 330 ± 27 (0.5%) nm; d,e) NP2 with an average edge length of 334 ± 111 (33%) nm; (g,h) NP3 with an average tip-to-tip length of 447 ± 65 (15%) nm. c,f,i) Size histograms for NP1, NP2 and NP3, respectively. Equivalent transmission electron microscopy (TEM) micrographs can be found in the SI, *cf.* section SI-VIII.

The influence of the solvent was also evaluated. After 45 min of reaction, followed by purification as described for NP1, the precipitate was redispersed in solvents having increasing polarity, that is, ethyl acetate, acetone (*i.e.*, NP1), N,N-dimethylformamide (DMF), acetonitrile, methanol, and ultrapure water (milliQ water). After redispersion in DMF, acetonitrile or methanol, followed by purification by centrifugation, sample color (brownish) and morphology resembled that of NP1 (*i.e.*, acetone), *cf*. Figure SI-II1 in SI, suggesting the material stability. In contrast, ethyl acetate triggered an immediate color (brownish to greenish) and morphology change (microstructures). If initially, samples redispersed in DMF, acetonitrile or methanol retained color and morphology similar to NP1, these samples experienced a change in color (brownish to violetish) and morphology over time, as shown by SEM inspection, *cf*. evolution of the samples redispersed in methanol over 72 h in SI (*cf.*, Figure SI-II2). Dispersion of NP1 or NP2 in MilliQ water produced a color (brownish to grayish) and morphology change, which evolved over time. If initially MilliQ water samples appeared as fibers in SEM, *cf.* Figure SI-II3, after 72 h in MilliQ water, the morphology of the complexes after purification resembles nanospikes (in the following referred to as NP3) with an average tip-to-tip length (L) of 447 ± 65 (15%) nm, *cf.* Figure 1(c), which remains colloidally stable (with no apparent color or morphology change by SEM inspection) over long periods of time (so far, up to months). This morphological aspect is comparable with that one of CuO nanowire/microflower recently reported.[55]

NP1, NP2 and NP3 exhibit a crystalline state characterized by long range order, with two types of Powder X-Ray Diffraction (PXRD) patterns, *cf.*, Figure 2. First, despite a slight difference in the

full width at half maximum (FWHM), NP1 and NP2 share an identical new structure, having main diffraction peaks at *ca.* 14.1, 14.5, 29.5, 33.1 and 48° 2θ. Structural resolution was however not possible due to the weak diffraction power as well as a small crystallite size. The different FWHM (see section SI-VII in SI) might be related with the larger crystal size of NP2, *cf.* Figure 1. The nanosheets of NP2 seem to be the ones detangled from the NP1 nanospheres as result of the thermodynamic crystallization.

In the second type of PXRD patterns, corresponding to NP3**,** coexists two crystalline phases: i) Bragg reflections at 14.4 and 29.7°, corresponding to the NP1/NP2 phase; and ii) diffraction peaks at 32.3, 35.5, 38.5 and 49° 2θ that can be assigned to the 110, 111, 200 and 202 Miller indices of the tenorite form of copper (II) oxide (*cf.*, Figure SI-VII),[55] coming probably from the partial transformation of NP1 into CuO due to the presence of Milli-Q water. This result is in total agreement with previous SEM observations.

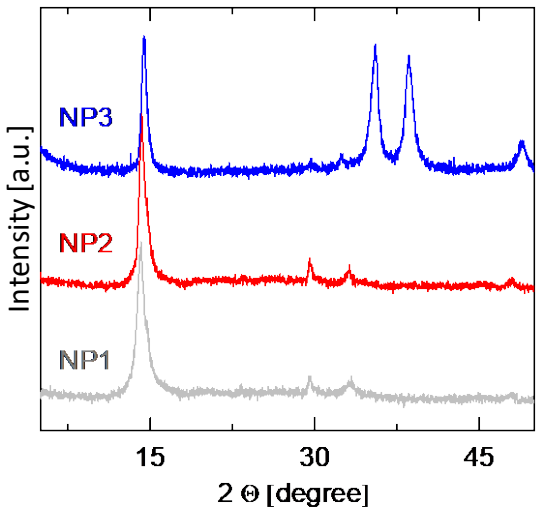


**Figure 2**. PXRD patters of NP1 (grey), NP2 (red), NP3 (blue).

Electron paramagnetic resonance (EPR) spectroscopy is a powerful technique to characterize the electronic structure of paramagnetic metal centers, such as $Cu^{2+}$ in metalloproteins,[56] MOFs,[57] and molecules.[58] In an EPR experiment, the unpaired electron spin of the $Cu^{2+}$ interacts with the magnetic field and the surrounding nuclear spins, thereby providing a spectrum with a characteristic pattern that resembles coordination ligands and geometry of the $Cu^{2+}$ complex. EPR spectroscopy is very sensitive to changes in the electronic configuration of a $Cu^{2+}$ center and thus, highly useful to inspect the species $Cu^{+2}$-2MI investigated here. Figure 3 shows the EPR spectra of NP1, NP2 and NP3 in frozen solutions (120 K), which include all possible orientations of an analogous single crystal with respect to the magnetic field. The three solids show the typical features of $Cu^{2+}$–imidazole complexes,[59] therefore demonstrating the formation of Cu-N bond in the three NPs. Due to the interaction of the unpaired electron spin of the $Cu^{2+}$ and its nuclear spin (3/2), the hyperfine pattern of each species exhibits three of the four hyperfine transitions in the parallel region of the spectra (low-field range, *i.e.*, four-arrow pattern in Figure 3) while the fourth component is masked by overlap with the hyperfine transitions in the perpendicular region and with “extra absorption” features towards the high-field end of the

spectra,[60] *cf.* Figure 3. In $Cu^{2+}$ complexes, nitrogen ligands can interact with the unpaired electron of the $Cu^{2+}$ and give rise to further splitting of the hyperfine pattern, *c.f.* Figure 3d, referred to as superhyperfine pattern, which accounts for the number of nitrogen ligands. Remarkably, the nine-line superhyperfine splitting (1.5 mT) is consistent with four strongly coordinating and largely equivalent nitrogen ligands in square planar coordination, as previously reported in Cu(II)-metalloproteins and tetrakisimidazolecopper(II) sulfate.[56,60,61] We speculatively associate better resolution of the superhyperfine splitting of NP2/NP3 in comparison with NP1 as indication of a more equivalent nitrogen-copper interaction (*i.e.*, similar bond distances and tetragonal distortion), resulting of the longer crystallization time and refinement of the structure after thermodynamic growth compared to kinetic growth of NP1/NP3.

In addition, these spectra present varying degrees of distortion due to $Cu^{+2}$-$Cu^{+2}$ dipolar coupling, particularly dominant in NP3, which is apparent in EPR powder (RT) of the three species, *cf.*, full-width spectra in section S9 of the SI. Table 1 gives numerical values of the four-arrow patterns depicted in Figure 3. EPR spectra of NP2 and NP3 are very similar, both regarding parameters listed in Table 2 and superhyperfine splitting (1.5 mT) towards the high-field end of the spectra. It is important to notice that copper (II) oxide, major component of NP3 as determined by PXRD, is EPR-silent due to extensive spin−spin among neighboring Cu(II) ions, which result in a diamagnetic ground state.[62] Therefore, the EPR signal observed in NP3 is in agreement with the presence of the Cu-N bonds related to $Cu^{2+}$complexes (likely as NP2), as previously discussed with the PXRD data.

**Table 2.** EPR parameters of X-band spectra of frozen solutions (120 K) of the three compounds.

| Sample | $g_{\parallel}$ | $A_{\parallel}$ (mT) |
|---|---|---|
| **NP1** | 2.28 | 16.7 |
| **NP2** | 2.26 | 17.2 |
| **NP3** | 2.26 | 17.2 |

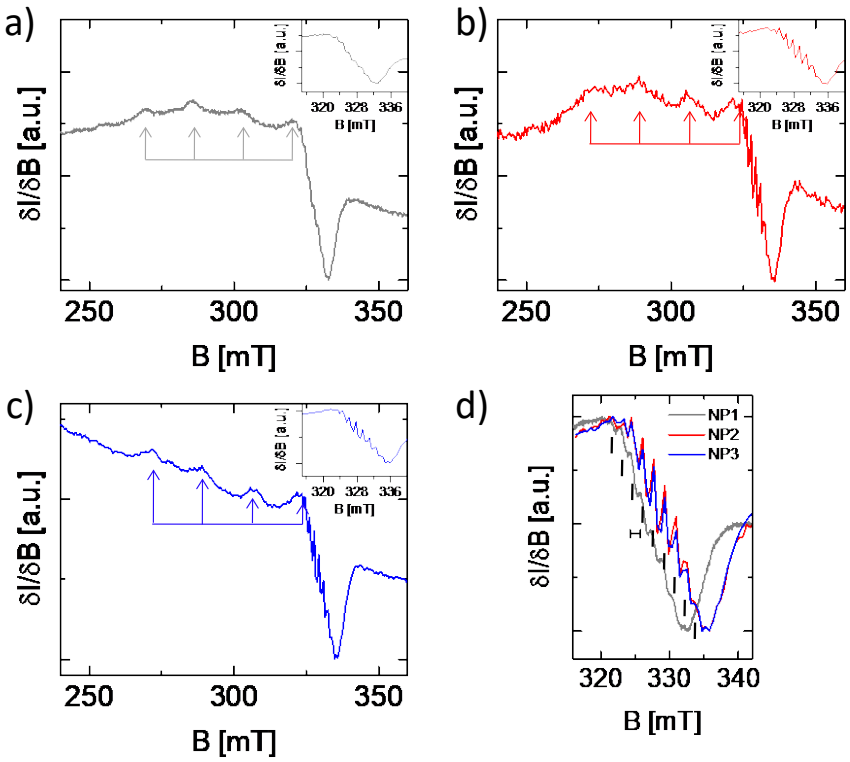


**Figure 3.** Frozen solution (120 K) EPR spectra of the species: a) NP1 (grey; acetone); b) NP2 (red; acetone); c) NP3 (blue; water); d) Hyperfine transitions in the perpendicular region of the three species having "extra absorption" features towards the high-field end of the spectra, *i.e.*, superhyperfine splitting due interaction of the unpaired electron of the $Cu^{2+}$ with nitrogen ligands. Nine discontinued lines homogeneously spaced (1.5 mT) point at this superhyperfine splitting.

Fourier-transform infrared spectroscopy (FTIR) also provides information of the structure of the Cu-2MI coordination polymers. FTIR spectra corroborate the presence of 2MI in NP1, NP2 and NP3, as shown by the characteristic 2MI bands, *cf.* asterisks in Figure 4. Most notably, the three NPs share bands of the 2MI linker at 1438 $cm^{-1}$ and 1296 $cm^{-1}$ due to C-N stretching, and at 1115 $cm^{-1}$ and between 900-700 $cm^{-1}$ due to C-H stretching. FTIR spectrum of the 3 solids are almost identical, with the exception of NP3, as it exhibits a broad bands around 3300 $cm^{-1}$ due to water absorption (-OH stretching), and at frequencies 610 and 515 $cm^{-1}$, which are ascribable to metal-oxygen vibrations, thereby confirming the presence of copper(II) oxide. The FTIR features of these three compounds match that of the ZIF-8,[27] as expected due to the use of the same linker 2MI. CTAB bands at 2915 and 2847 $cm^{-1}$ are caused by the C−H stretching vibration of methyl and methylene groups. In the case of the three NPs, the band at 2847 $cm^{-1}$ seems to vanish, while the band at 2915 $cm^{-1}$, characteristic of C-H stretching of methyl groups in ZIF-8 solids, remains. Although we cannot rule out the presence of CTAB, it is unlikely due to the low CTAB concentration used during the synthesis (*i.e.*, below critical micelle concentration; 2MI:CTAB molar ratio of 1000:1) and centrifugal purifications with MilliQ water and acetone.

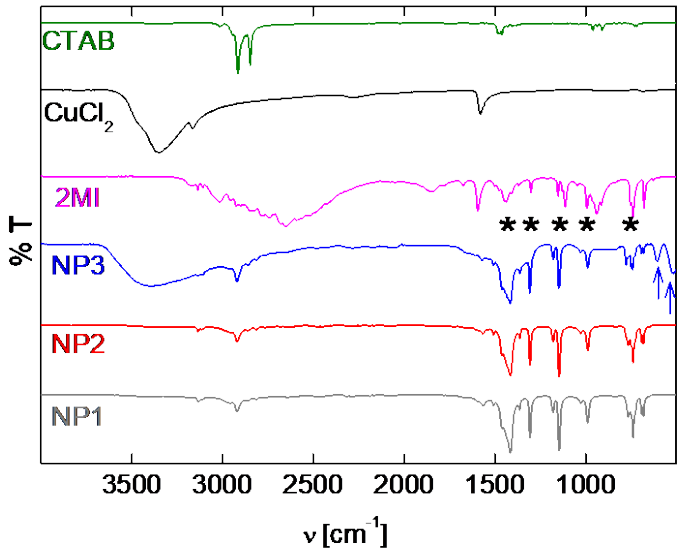


**Figure 4.** FTIR spectra of the starting reactants and the three NPs obtained. Asterisks point at 2MI bands (pink) that are observed in NP1 (grey), NP2 (red) and NP3 (blue). Blue arrows point at metal-oxygen vibrations in NP3.

In order to investigate the thermal behavior of NP1, both thermogravimetric analysis (TGA) and temperature dependent PXRD experiments were performed under air atmosphere. TGA curve (Figure 5) shows two weight losses: a first sharp mass loss (~20 wt%) at around 220 °C, and then, a progressive weight loss (~50 wt%) between 250 and 700 °C, associated with the total combustion of 2MI and the final formation of CuO (~30 wt%). Note here that the first weight loss is assigned to the departure of 2MI ligand considering that free ligand is removed from 150 to 200 °C (see Figure SI-VI). The higher departure temperature of the ligand within the solid is in agreement with the formation of interactions with Cu (as previously proved by EPR), observing two types of ligand fractions (departure at 220 and >250 °C) which might be interacting in a different manner. Further, as observed by temperature dependent PXRD (Figure 5), the initial ligand departure leads to the collapse and amorphization of the crystalline framework, being the NP1 solid thermally stable up to around 200 °C. Previous thermo-diffraction analysis done to ZIF-8 under air reveal that its structure remains stable up to 300 °C, while NP1 only withstand 200 °C.[63] Nevertheless, similar experiments carried out with HKUST-1 revealed similar thermal stability compared to NP1, as the structure starts degradation after 150 °C and becomes completely amorphous after 200 °C under air.[64]

TGA curves of NP2 show a similar behavior than NP1 with however a lower weight loss at 220 °C (20 *vs*. 25 wt%; *cf.*, Figure 5). From TGA and elemental analysis, the chemical formula $Cu(C_4H_5N_2)_2$ (theo: C=42.5, N=24.8, H=4.5 and Cu=28.2 %) is proposed for NP1 or NP2 (exp: C = 41.5, N = 24.2, H = 4.4, Cu = 24 % for NP1 and C = 42.3, N = 25.53, H = 4.3, Cu=29 % for NP2). The better correlation with the proposed formula of NP2 might be a result of its better crystallization. Finally, TGA of NP3 sample exhibits a similar profile with a higher content of remaining CuO, in agreement with the presence of this oxide because of the partial degradation of NP1 in water.

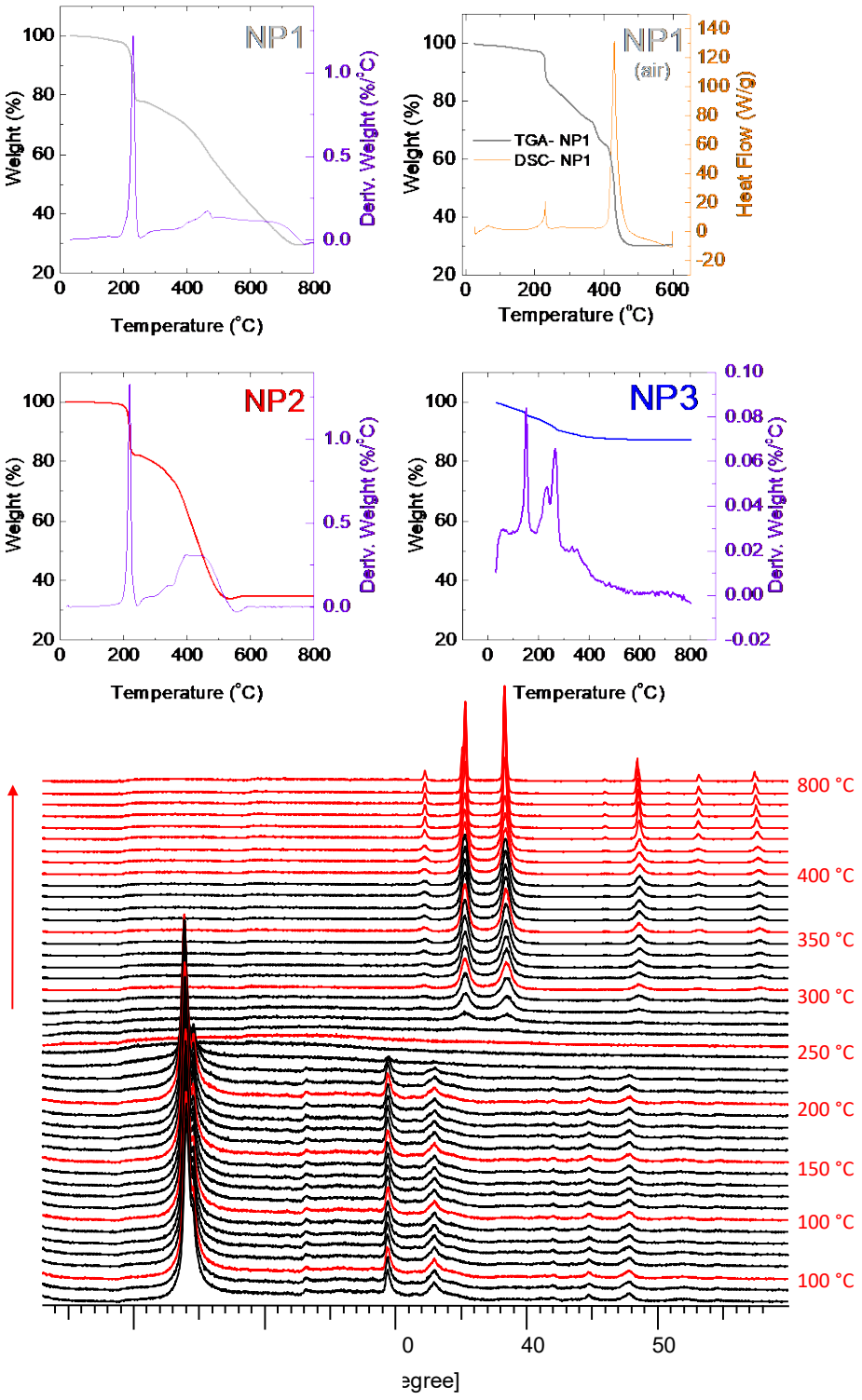


**Figure 5**. TGA of the NPs: a) NP1 in $N_2$ (grey); b) NP1 in air (grey); c) NP2 in $N_2$ (red); d) NP3 in $N_2$ (blue). Violet lines correspond to the first derivative of the TGA curves (a, c and d) and the orange line corresponds to the DSC of sample NP1 (air) (b), indicating the rate of temperature degradation. d) Temperature dependent PXRD experiment carried out with NP1.

$N_2$ sorption measurements at 77K of NP1, NP2 and NP3 show type I isotherms *(cf.*, Figure 6), characteristic of microporous materials, with a Brunauer, Emmett & Teller(BET; $P/P_o<0.15$)

specific surface areas of 144, 86 and 53 $m^2 \cdot g^{-1}$, respectively. Although exhibiting a $N_2$ accessible microporosity, BET surface is quite low with respect to other imidazolate-based (ZIF-8(Zn):$S_{BET}$ = 1800 $m^2 \cdot g^{-1}$)[53] or Cu-based MOFs (Cu trimesate HKUST-1: $S_{BET}$ = 1100 $m^2 \cdot g^{-1}$).[49,65] The higher surface of NP1 with respect to NP2 could be related with the presence of defects, in consonance with the better crystallization of the solid after 72 h of reaction, and agrees with the results of PXRD and EPR. Further, the additional continuous $N_2$ adsorption at higher relative pressures ($P/P_o$>0.2) might correspond to the adsorption on the outer surface of the NPs, being more important in the smaller entangled-nanosheets of NP1 than in NP2, with larger crystal size. In both samples, the porosity is associated to a pore size distribution of around 1 nm-diameter (estimated by the Horváth-Kawazoe -HK method). Finally, NP3 possesses the lowest surface area, $S_{BET}$ = 53 $m^2 \cdot g^{-1}$, and might be explained by the partial degradation of the NP1 to the dense CuO phase ($S_{BET}$ = 4 $m^2 \cdot g^{-1}$).[66]

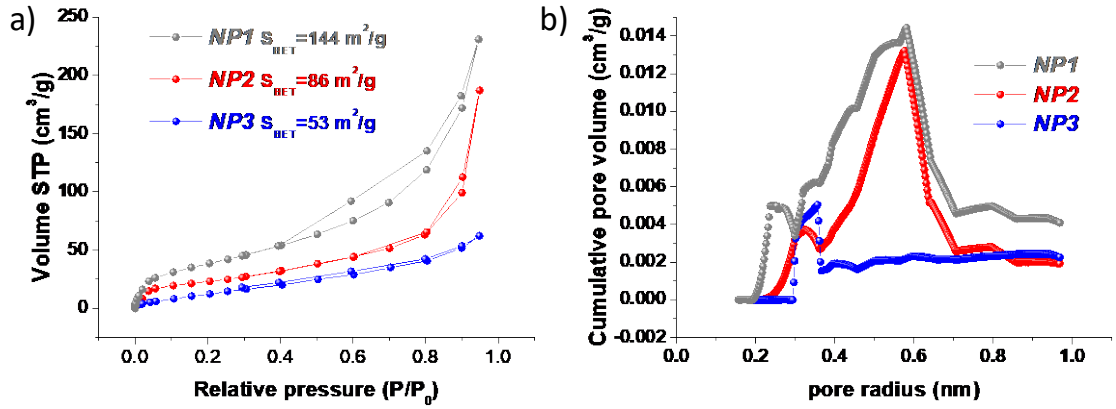


**Figure 6.** $N_2$ sorption isotherms (a) and HK pore volume distribution (b) of NP1 (grey), NP2 (red) and NP3 (blue)

Basic physicochemical properties of NP1 (acetone), NP2 (acetone) and NP3 (MilliQ water) in solution were investigated, including UV-Vis and fluorescence spectroscopy, and dynamic light scattering (DLS). Upon storage at 4 °C, the NPs were colloidally stable over extended periods of time (months), with no apparent change of color or morphology, *cf*. insets in Figure 1. UV-Vis-NIR spectrum of NP2 shows a narrow absorption band centered at 380 nm, which broadens in NP1, and even further in NP3, in which a broad absorption in the range 300 – 900 nm dominates, *cf*. Figure 7(a). The spectra of NP1 and NP2 (*i.e.*, band at 380 nm) show no clear similarities with those of the precursors (*cf*. Figure SI-III) or other Cu-NMOFs, $Cu_2O$ or CuO nanostructures[66,67] or Cu(II)-histidine complexes.[68] In contrast, the spectrum of NP3 resembles that of CuO nanosheets previously reported.[69] Fluorescence spectroscopy of NP1, NP2 and NP3 shows no significant fluorescence emission, *cf.* Figure SI-IV. The hydrodynamic size of the NPs was evaluated by DLS, which show the same trend as SEM inspection, *cf*. Figure 7(b). DLS raw data are given in the SI (*cf.* section SI-V). In addition, low polydispersity indexes (PDI) were found for NP1 (0.04), which in the case of NP2 and NP3 were larger (0.46 and 0.36, respectively), *cf*. Figure 7(b), as expected from SEM analysis.

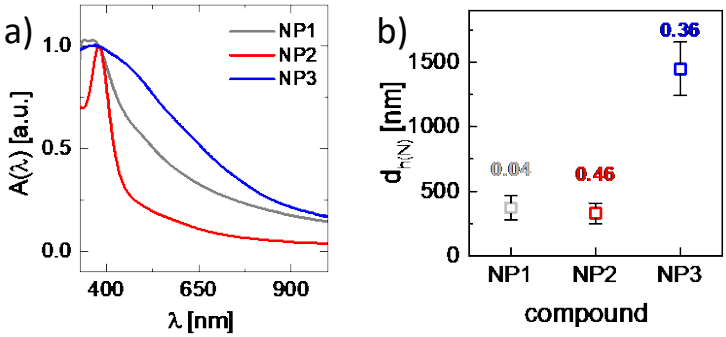


**Figure 7.** Colloidal characterization of the species: (a) UV-Vis spectra of NP1 (grey; in acetone), NP2 (red; in acetone) and NP3 (blue; in MilliQ water); (b) Mean average hydrodynamic diameter obtained from the DLS number distribution of NP1 (grey; in acetone), NP2 (red; in acetone) and NP3 (blue; in MilliQ water). Colored values above the hollow squares correspond to PDI values.

In agreement with the results presented above, the main outcomes of this green bottom-up synthesis of the three NPs are briefed: i) a new crystalline structure of a copper imidazolate has been synthesized, ii) the formation of a strong interactions between the $Cu^{2+}$ inorganic building units and the 2-MI ligands has been demonstrated by EPR, iii) the synthesized NPs possess high monodispersity and colloidal stability in acetone and water with a tuned morphology, iv) the NPs exhibit thermal stability up to 200 °C and iv) they exhibit a moderate microporosity associated to 1 nm-diameter pores. Thus, one can conclude that these properties are in correspondence with those attributed to the previous definition of nanoPCPs.

As a proof of concept, catalytic activity of the three NPs was assayed towards their capability to trigger the reduction of methylene blue (MB, blue) into leucomethylene blue (LB, colorless) in MeOH in the presence of $NaBH_4$. In order to make a fair comparison among NPs, reactions were performed keeping the copper mass constant (*i.e.*, 1.9 ng). The concentration of stock solutions of the three solids was determined by a classic colorimetric method (*i.e.*, production of the blue compound $Cu(NH_3)_4^{2+}$) and confirmed by inductively coupled plasma mass spectrometry (ICP-MS), *cf.* Section SI-X in SI. The reduction of MB into LB was followed by collecting the absorbance at 664 nm (A) during 100 s (one measurement per s),[70] *cf*. Figure 8. The catalytic properties of the three solids were calculated by kinetics ($k$, Ln ($A/A_0$)), taking into account the initial 22 s of reaction, *cf*. Table 3. That is, $k$ [$s^{-1}$] is obtained from the slope of the curves Ln ($A/A_0$) *vs* time. The blank absorption (ctrl) was measured using the same parameters but in presence of MeOH instead of the sample (NP1, NP2 and NP3) solution.

As expected, the species NP1 and NP2 present significantly higher catalytic properties (*i.e.*, high $k$) than the low-porosity NP3 or the control sample. The obtained $k$ values are in the order of previous reports using equivalent catalytic reactions.[71,72] However, these values are not fully comparable due to different experimental conditions, including the solvent used (water or methanol), and the amount of $NaBH_4$ used, in our case *ca.* 12 times lower than previous reports.[71,72] Remarkably and despite those experimental differences, it is worth mentioning that in our case, the amount of material used *per* experiment is in the ng order, while in the previously discussed works, it is in the µg range. This fact points out the high catalytic activity of our systems under these conditions.

**Table 3.** Summary of the kinetic constant values $k$ [$s^{-1}$] for the selected samples (equal Cu mass – 1.9 ng) and control (without Cu). A first-order catalytic behavior was considered, *i.e.*, $\mathrm{Ln}(A/A_0) = -k \cdot t$, during the initial 22 s of the reaction.

| Sample | $k$ ($s^{-1}$) |
|---|---|
| **NP1** | $53.7 \cdot 10^{-3} \pm 1.2 \cdot 10^{-3}$ |
| **NP2** | $67.6 \cdot 10^{-3} \pm 0.3 \cdot 10^{-3}$ |
| **NP3** | $2.6 \cdot 10^{-3} \pm 1.6 \cdot 10^{-5}$ |
| **ctrl** | $2.6 \cdot 10^{-3} \pm 1.7 \cdot 10^{-5}$ |

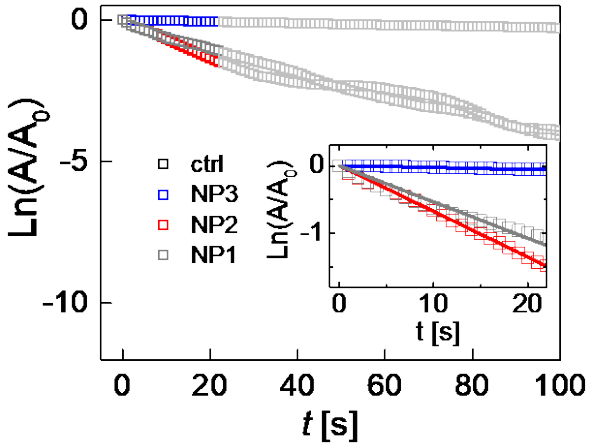


**Figure 8.** Absorbance at 664 nm (A) versus time for equal mass of copper, *i.e.*, NP1 (grey), NP2 (red) and NP3 (blue), and control sample (ctrl, black). $A_0$ is the absorption at 664 nm at time 0 s. Data considered for the kinetic fitting (first order) are colored (initial 22 s). Insets show zoom areas of the fitting regions for selected samples and control.

## CONCLUSIONS

A bottom-up green chemical method for the preparation of a new nanometric microporous coordination polymer (*i.e.*, NP1/NP2) has been described. A molar ratio 2MI:$Cu^{2+}$ of 20 (and 2MI:CTAB of $10^3$) was found as optimum for the production of highly monodisperse nanospheres (NP1; 330 ± 27 (0.5%) nm), which resemble an entangled network of very thin nanosheets (< 10 nm). NP1 was produced within 45 min of reaction. However, if the reaction is left to proceed for 72 h or longer (instead of 45 min), a morphology change occurs, and larger nanosheets (NP2; edge length of 334 ± 111 (33%) nm) were produced instead. The colloidal stability of these solids in different solvent was evaluated, being acetone the most suitable one because it does not affect the colloidal, chemical and structural integrity of the solids over extensive periods of time (months). The redispersion of NP1 in aqueous solution triggered a morphology change, initiated with the formation of nanofibers, which evolved into nanospikes (NP3; average length of 447 ± 65 (15%) nm) in the course of 72 h.

The physicochemical, structural and catalytic properties of these three solids were evaluated. NP1 and NP2, although morphologically different, present similar properties with regards to crystalline structure, porosity and catalytic activity, highlighting here a remarkable catalytic activity in the reduction of methylene blue. In contrast, NP3 seems to be a degradation product of NP1, mainly composed of copper oxide, although it also contains a $Cu^{2+}$-2MI porous phase.

**EXPERIMENTAL SECTION**

*Chemicals*: Copper(II) chloride dihydrate ($CuCl_2 \cdot 2H_2O$ 99.999%, molecular weight MW= 170.48 $g \cdot mol^{-1}$) was purchased from Stream Chemicals; hexadecyltrimethylammonium bromide (CTAB, 98%, MW = 364.45 $g \cdot mol^{-1}$) and 2-methylimidazole (2MI, 99%, MW = 82.10 $g \cdot mol^{-1}$) were purchased from Sigma-Aldrich. All materials were used as received without further purification. Milli-Q water (18.2 MΩ cm) was used in all the experiments.

*Characterization*: Optical characterization in solution was performed using a Biochrom Libra S60 UV–visible spectrophotometer. Fluorescence characterization in solution was performed using a Horiba FluoroMax-3 spectrometer. Thermogravimetric analysis (TGA) of powder samples was performed using a TA Instruments Inc. Q5000 operating in nitrogen with sample purge gas flow of 25 $mL \cdot min^{-1}$, or air, and samples scanned at a heating rate of 10 °C·$min^{-1}$ from 30 to 800 °C. Elemental analysis was carried out in a Flash 2000 analyser from Thermo Scientific. Fourier-transform infrared spectroscopy (FTIR) of powder samples was performed using a Perkin-Elmer Two equipped with ATR; samples were scanned from 550–3500 $cm^{-1}$. A X-ray diffractometer Philips was used to study the crystalline powder of samples; the samples were examined in the range of 2θ between 2° and 75°, with a passage of 0.02° and a time by step of 2s. X-ray thermodiffraction experiment was performed using a D8 Advance Bruker AXS θ-2θ diffractometer equipped with a LYNXEYE XE detector with a copper radiation source (Cu Kα, λ =1.5406 Å), and an Anton Paar XRK 900 high-temperature chamber. Data were collected under synthetic air atmosphere (10 $mL \cdot min^{-1}$) in the 2θ range 4-60° and in the temperature range of 30-800°C at 10°C intervals. NP hydrodynamic size and polydispersity index (PDI) were determined by dynamic light scattering (DLS) using a Malvern Zetasizer Nano ZSP. TEM images were acquired with a HRTEM Libra 200 FE OMEGA operated at 200 kV. SEM images were acquired with a FESEM Zeiss Ultra Plus operated at 3 kV. Inductively coupled plasma mass spectrometry (ICP-MS) was performed using an ICP-MS cuadrupolar Agilent 7700x. Electron paramagnetic resonance (EPR) spectroscopy was performed using a CW X-band EPR Bruker EMX spectrometer. $N_2$ sorption isotherms (77 K) were done in an AUTO-SORB system (Quantachrome Instruments). Prior to the measurement, the sample was evacuated at 50 °C for 16 h. Specific surface was determined applying BET equation (Brunauer, Emmett & Teller) in the pressure interval P/Po =0.02-0.15 (being $P_0$ the saturation pressure). Pore size distribution was calculated by the HK method (Horvath-Kawazoe).

*Synthesis of nanocomposites*: Typically, 1 mL of an aqueous solution of 2MI (1 M) and 1 mL of an aqueous solution of CTAB (1 mM) were added simultaneously to 1 mL of an aqueous solution of $CuCl_2 \cdot 2H_2O$ (different concentrations, *cf*. Table 1). The reaction may be scaled at least up to 30 mL (*i.e.*, 10 mL instead of 1 mL of each reactant) with equivalent results.

The solution was gently stirred for 1 min in which the color of the solutions changed from bluish to brownish (*cf.* Figure 1). Then, the solution was left undisturbed for 45 min at room temperature (RT). The resulting nanocomposites were purified by centrifugation (7000 rcf, 15 min), the supernatant was discarded and the precipitate was redispersed either in 3 mL of water or 3 mL of acetone (other solvents such as methanol, acetonitrile, ethyl acetate and dimethylformamide were tested, *cf*. SI). Unless otherwise specified, all the characterization data presented in this manuscript refers to sample Cu50, which showed best monodispersity among all samples.

*Reduction of methylene blue (MB, blue) into leucomethylene blue (LB, colorless) in MeOH*: 970 µL of MeOH were mixed with 15 µL of MB from a stock solution ($9.37 \cdot 10^{-4}$ M, MeOH). Then, 5 µL of freshly prepared solution of $NaBH_4$(130 mM, MeOH) and 5 µL of sample (1.9ng Cu, MeOH) or MeOH (control) were added.

**Acknowledgments:** This work has received financial support from the Spanish MINECO-AEI/FEDER, UE (MAT2016-80266-R to PT, MAT2015–74381-JIN to BP, CTQ2017-89588-R to PdP and ENE2016-79608-C2-1-R to PH), the Xunta de Galicia (Centro singular de investigación de Galicia accreditation 2016–2019, ED431G/09) and the European Union (European Regional Development Fund - ERDF). PH and PdP acknowledge the RyC program (grant agreement n° 2014-16823 and 2014-16962). MFNP acknowledges the CONACYT PhD fellowship program.

**Supporting Information Available:** Additional data regarding optimization of 2MI:$Cu^{2+}$ molar ratio (SI-I), colloidal stability in different solvents (SI-II), UV-VIS spectroscopy (SI-III), fluorescence spectroscopy (SI-IV), dynamic light scattering (SI-V), thermogravimetric analysis (SI-VI), powder x-ray diffraction (SI-VII), transmission electron microscopy (SI-VIII), electron paramagnetic resonance (SI-IX) and copper concentration determination (SI-X). This material is available free of charge via the Internet at http://pubs.acs.org.

**REFERENCES**


1. Seth, S.; Matzger, A. J. Metal–organic frameworks: examples, counterexamples, and an actionable definition. *Cryst. Growth Des.* **2017**, *17*, 4043-4048.
2. Howarth, A. J.; Liu, Y. Y.; Li, P.; Li, Z. Y.; Wang, T. C.; Hupp, J.; Farha, O. K. Chemical, thermal and mechanical stabilities of metal-organic frameworks. *Nat. Rev. Mater.* **2016**, *1,* 15018.
3. Zhu, Q.-L.; Xu, Q. Metal-organic framework composites. *Chem. Soc. Rev.* **2014**, *43*, 5468-5512.
4. Maurin, G.; Serre, C.; Cooper, A.; Ferey, G. The new age of MOFs and of their porous-related solids. *Chem. Soc. Rev.* **2017**, *46*, 3104-3107.
5. Tominaka, S.; Hamoudi, H.; Suga, T.; Bennett, T. D.; Cairns, A. B.; Cheetham, A. K. Topochemical conversion of a dense metal-organic framework from a crystalline insulator to an amorphous semiconductor. *Chem. Sci.* **2015**, *6*, 1465-1473.
6. McDonald, K. A.; Seth, S.; Matzger, A. J. Coordination polymers with high energy density: an emerging class of explosives. *Cryst. Growth Des.* **2015**, *15*, 5963-5972.
7. Cui, Y.; Li, B.; He, H.; Zhou, W.; Chen, B.; Qian, G. Metal–organic frameworks as platforms for functional materials. *Acc. Chem. Res.* **2016**, *49*, 483-493.
8. Furukawa, H.; Cordova, K. E.; O'Keeffe, M.; Yaghi, O. M. The chemistry and applications of metal-organic frameworks. *Science* **2013**, *341*.
9. Yaghi, O. M.; O'Keeffe, M.; Ockwig, N. W.; Chae, H. K.; Eddaoudi, M.; Kim, J. Reticular synthesis and the design of new materials. *Nature* **2003**, *423*, 705-714.
10. Yaghi, O. M.; Li, G.; Li, H. Selective binding and removal of guests in a microporous metal-organic framework. *Nature* **1995**, *378*, 703-706.
11. Li, H.; Eddaoudi, M.; O'Keeffe, M.; Yaghi, O. M. Design and synthesis of an exceptionally stable and highly porous metal-organic framework. *Nature* **1999**, *402*, 276-279.
12. Riou, D.; Roubeau, O.; Férey, G. Composite microporous compounds. Part I: Synthesis and structure determination of two new vanadium alkyldiphosphonates (MIL-2 and MIL-3) with three-dimensional open frameworks. *Micropor. Mesopor. Mat.* **1998**, *23*, 23-31.
13. Hoskins, B. F.; Robson, R. Infinite polymeric frameworks consisting of three dimensionally linked rod-like segments. *J. Am. Chem. Soc.* **1989**, *111*, 5962-5964.
14. Kondo, M.; Yoshitomi, T.; Matsuzaka, H.; Kitagawa, S.; Seki, K. Three-dimensional framework with channeling cavities for small molecules: {[M2(4, 4'-bpy)3(NO3)4]·xH2O}n (M = Co, Ni, Zn). *Angew. Chem. Int. Ed.* **1997**, *36*, 1725-1727.
15. Nasalevich, M. A.; Goesten, M. G.; Savenije, T. J.; Kapteijn, F.; Gascon, J. Enhancing optical absorption of metal-organic frameworks for improved visible light photocatalysis. *Chem. Commun.* **2013**, *49*, 10575-10577.
16. Stylianou, K. C.; Imaz, I.; Maspoch, D. Metal-organic frameworks: nanoscale frameworks. In *Encyclopedia of Inorganic and Bioinorganic Chemistry*, John Wiley & Sons, R. A. Scott (Ed.), **2014**.
17. Makiura, R.; Motoyama, S.; Umemura, Y.; Yamanaka, H.; Sakata, O.; Kitagawa, H. Surface nano-architecture of a metal–organic framework. *Nat. Mater.* **2010**, *9*, 565-571.
18. Green, M. A. Crystal engineering in two dimensions: Surface attraction. *Nat. Mater.* **2010**, *9*, 539-540.
19. Zheng, G.; de Marchi, S.; López-Puente, V.; Sentosun, K.; Polavarapu, L.; Pérez-Juste, I.; Hill, E. H.; Bals, S.; Liz-Marzán, L. M.; Pastoriza-Santos, I.; Pérez-Juste, J. Encapsulation of single plasmonic nanoparticles within zif-8 and sers analysis of the mof flexibility. *Small* **2016**, *12*, 3935-3943.
20. Wang, Z.; Tang, X.; Wang, X.; Yang, D.; Yang, C.; Lou, Y.; Chen, J.; He, N. Near-infrared light-induced dissociation of zeolitic imidazole framework-8 (ZIF-8) with encapsulated CuS nanoparticles and their application as a therapeutic nanoplatform. *Chem. Commun.* **2016**, *52*, 12210-12213.

21. He, L.; Brasino, M.; Mao, C.; Cho, S.; Park, W.; Goodwin, A. P.; Cha, J. N. dna-assembled core-satellite upconverting-metal–organic framework nanoparticle superstructures for efficient photodynamic therapy. *Small* **2017**, *13*, 1700504-n/a.
22. Borges, M.; Yu, S.; Laromaine, A.; Roig, A.; Suarez-Garcia, S.; Lorenzo, J.; Ruiz-Molina, D.; Novio, F. Dual T1/T2 MRI contrast agent based on hybrid SPION@coordination polymer nanoparticles. *RSC Adv.* **2015**, *5*, 86779-86783.
23. Hu, P.; Morabito, J. V.; Tsung, C.-K. Core–shell catalysts of metal nanoparticle core and metal–organic framework shell. *ACS Catal.* **2014**, *4*, 4409-4419.
24. El-Shall, M. S.; Abdelsayed, V.; Khder, A. E. R. S.; Hassan, H. M. A.; El-Kaderi, H. M.; Reich, T. E. Metallic and bimetallic nanocatalysts incorporated into highly porous coordination polymer MIL-101. *J. Mater. Chem.* **2009**, *19*, 7625-7631.
25. Lin, W.; Rieter, W. J.; Taylor, K. M. L. Modular synthesis of functional nanoscale coordination polymers. *Angew. Chem. Int. Ed.* **2009**, *48*, 650-658.
26. Kuo, C.-H.; Tang, Y.; Chou, L.-Y.; Sneed, B. T.; Brodsky, C. N.; Zhao, Z.; Tsung, C.-K. Yolk–shell nanocrystal@zif-8 nanostructures for gas-phase heterogeneous catalysis with selectivity control. *J. Am. Chem. Soc.* **2012**, *134*, 14345-14348.
27. Lu, G.; Li, S.; Guo, Z.; Farha, O. K.; Hauser, B. G.; Qi, X.; Wang, Y.; Wang, X.; Han, S.; Liu, X.; DuChene, J. S.; Zhang, H.; Zhang, Q.; Chen, X.; Ma, J.; Loo, S. C. J.; Wei, W. D.; Yang, Y.; Hupp, J. T.; Huo, F. Imparting functionality to a metal–organic framework material by controlled nanoparticle encapsulation. *Nat. Chem.* **2012**, *4*, 310-316.
28. Horcajada, P.; Chalati, T.; Serre, C.; Gillet, B.; Sebrie, C.; Baati, T.; Eubank, J. F.; Heurtaux, D.; Clayette, P.; Kreuz, C.; Chang, J.-S.; Hwang, Y. K.; Marsaud, V.; Bories, P.-N.; Cynober, L.; Gil, S.; Ferey, G.; Couvreur, P.; Gref, R. Porous metal-organic-framework nanoscale carriers as a potential platform for drug delivery and imaging. *Nat. Mater.* **2010**, *9*, 172-178.
29. Wang, X.-G.; Dong, Z.-Y.; Cheng, H.; Wan, S.-S.; Chen, W.-H.; Zou, M.-Z.; Huo, J.-W.; Deng, H.-X.; Zhang, X.-Z. A multifunctional metal-organic framework based tumor targeting drug delivery system for cancer therapy. *Nanoscale* **2015**, *7*, 16061-16070.
30. Abánades Lázaro, I.; Haddad, S.; Sacca, S.; Orellana-Tavra, C.; Fairen-Jimenez, D.; Forgan, R. S. Selective surface pegylation of uio-66 nanoparticles for enhanced stability, cell uptake, and ph-responsive drug delivery. *Chem* **2017**, *2*, 561-578.
31. Orellana-Tavra, C.; Haddad, S.; Marshall, R. J.; Abánades Lázaro, I.; Boix, G.; Imaz, I.; Maspoch, D.; Forgan, R. S.; Fairen-Jimenez, D. Tuning the endocytosis mechanism of zr-based metal–organic frameworks through linker functionalization. *ACS Appl. Mater. Interfaces* **2017**, *9*, 35516-35525.
32. Schaate, A.; Roy, P.; Godt, A.; Lippke, J.; Waltz, F.; Wiebcke, M.; Behrens, P. Modulated synthesis of zr-based metal–organic frameworks: from nano to single crystals. *Chem. Eur. J.* **2011**, *17*, 6643-6651.
33. Zhao, M.; Wang, Y.; Ma, Q.; Huang, Y.; Zhang, X.; Ping, J.; Zhang, Z.; Lu, Q.; Yu, Y.; Xu, H.; Zhao, Y.; Zhang, H. Ultrathin 2d metal–organic framework nanosheets. *Adv. Mater.* **2015**, *27*, 7372-7378.
34. Vaucher, S.; Li, M.; Mann, S. Synthesis of prussian blue nanoparticles and nanocrystal superlattices in reverse microemulsions. *Angew. Chem. Int. Ed.* **2000**, *39*, 1793-1796.
35. Wee, L. H.; Lohe, M. R.; Janssens, N.; Kaskel, S.; Martens, J. A. Fine tuning of the metal-organic framework Cu3(BTC)2 HKUST-1 crystal size in the 100 nm to 5 micron range. *J. Mater. Chem.* **2012**, *22*, 13742-13746.
36. Diring, S.; Furukawa, S.; Takashima, Y.; Tsuruoka, T.; Kitagawa, S. Controlled multiscale synthesis of porous coordination polymer in nano/micro regimes. *Chem. Mater.* **2010**, *22*, 4531-4538.
37. Park, J.; Jiang, Q.; Feng, D.; Mao, L.; Zhou, H.-C. Size-controlled synthesis of porphyrinic metal–organic framework and functionalization for targeted photodynamic therapy. *J. Am. Chem. Soc.* **2016**, *138*, 3518-3525.

38. Li, P.; Klet, R. C.; Moon, S.-Y.; Wang, T. C.; Deria, P.; Peters, A. W.; Klahr, B. M.; Park, H.-J.; Al-Juaid, S. S.; Hupp, J. T.; Farha, O. K. Synthesis of nanocrystals of Zr-based metal-organic frameworks with csq-net: significant enhancement in the degradation of a nerve agent simulant. *Chem. Commun.* **2015**, *51*, 10925-10928.
39. Hirschle, P.; Prei; Auras, F.; Pick, A.; Volkner, J.; Valdeperez, D.; Witte, G.; Parak, W. J.; Radler, J. O.; Wuttke, S. Exploration of MOF nanoparticle sizes using various physical characterization methods - is what you measure what you get? *CrystEngComm* **2016**, *18*, 4359-4368.
40. Giménez-Marqués, M.; Hidalgo, T.; Serre, C.; Horcajada, P. Nanostructured metal–organic frameworks and their bio-related applications. *Coord. Chem. Rev.* **2016**, *307*, 342-360.
41. Nune, S. K.; Thallapally, P. K.; Dohnalkova, A.; Wang, C.; Liu, J.; Exarhos, G. J. Synthesis and properties of nano zeolitic imidazolate frameworks. *Chem. Commun.* **2010**, *46*, 4878-4880.
42. Zaera, F. Nanostructured materials for applications in heterogeneous catalysis. *Chem. Soc. Rev.* **2013**, *42*, 2746-2762.
43. Xiao, B.; Yuan, Q.; Williams, R. A. Exceptional function of nanoporous metal organic framework particles in emulsion stabilisation. *Chem. Commun.* **2013**, *49*, 8208-8210.
44. Ranft, A.; Betzler, S. B.; Haase, F.; Lotsch, B. V. Additive-mediated size control of MOF nanoparticles. *CrystEngComm* **2013**, *15*, 9296-9300.
45. Jiang, D.; Mallat, T.; Krumeich, F.; Baiker, A. Polymer-assisted synthesis of nanocrystalline copper-based metal–organic framework for amine oxidation. *Catal. Commun.* **2011**, *12*, 602-605.
46. Sanz, R.; Martinez, F.; Orcajo, G.; Wojtas, L.; Briones, D. Synthesis of a honeycomb-like Cu-based metal-organic framework and its carbon dioxide adsorption behaviour. *Dalton Trans.* **2013**, *42*, 2392-2398.
47. Chen, Z.; Xiang, S.; Arman, H. D.; Li, P.; Tidrow, S.; Zhao, D.; Chen, B. A Microporous metal–organic framework with immobilized –oh functional groups within the pore surfaces for selective gas sorption. *Eur. J. Inorg. Chem.* **2010**, *2010*, 3745-3749.
48. Chen, Y.; Wang, B.; Wang, X.; Xie, L.-H.; Li, J.; Xie, Y.; Li, J.-R. A Copper(II)-paddlewheel metal–organic framework with exceptional hydrolytic stability and selective adsorption and detection ability of aniline in water. *ACS Appl. Mater. Interfaces* **2017**, *9*, 27027-27035.
49. Chui, S. S.-Y.; Lo, S. M.-F.; Charmant, J. P. H.; Orpen, A. G.; Williams, I. D. A chemically functionalizable nanoporous material $[Cu_3(TMA)_2(H_2O)_3]_n$. *Science* **1999**, *283*, 1148-1150.
50. Karahan, Ö.; Biçer, E.; Taşdemir, A.; Yürüm, A.; Gürsel, S. A. Development of efficient copper-based mof-derived catalysts for the reduction of aromatic nitro compounds. *Eur. J. Inorg. Chem.*, **2018**, *2018*, 1073-1079.
51. Masciocchi, N.; Bruni, S.; Cariati, E.; Cariati, F.; Galli, S.; Sironi, A. Extended polymorphism in copper(ii) imidazolate polymers: a spectroscopic and xrpd structural study. *Inorg. Chem.* **2001**, *40*, 5897-5905.
52. Luz, I.; Corma, A.; Llabres i Xamena, F. X. Cu-MOFs as active, selective and reusable catalysts for oxidative C-O bond coupling reactions by direct C-H activation of formamides, aldehydes and ethers. *Catal. Sci. Technol.* **2014**, *4*, 1829-1836.
53. Park, K. S.; Ni, Z.; Côté, A. P.; Choi, J. Y.; Huang, R.; Uribe-Romo, F. J.; Chae, H. K.; O'Keeffe, M.; Yaghi, O. M. Exceptional chemical and thermal stability of zeolitic imidazolate frameworks. *Proc. Natl. Acad. Sci. U.S.A.* **2006**, *103*, 10186-10191.
54. Zheng, G.; Chen, Z.; Sentosun, K.; Perez-Juste, I.; Bals, S.; Liz-Marzan, L. M.; Pastoriza-Santos, I.; Perez-Juste, J.; Hong, M. Shape control in ZIF-8 nanocrystals and metal nanoparticles@ZIF-8 heterostructures. *Nanoscale* **2017**, *9*, 16645-16651.
55. Wang, X.; Yang, J.; Shi, L.; Gao, M. Surfactant-free Synthesis of CuO with Controllable Morphologies and Enhanced Photocatalytic Property. *Nanoscale Res. Lett.* **2016**, *11*, 125.
56. del Pino, P.; Weiss, A.; Bertsch, U.; Renner, C.; Mentler, M.; Grantner, K.; Fiorino, F.; Meyer-Klaucke, W.; Moroder, L.; Kretzschmar, H. A.; Parak, F. G. The configuration of the Cu2+ binding region in full-length human prion protein. *Eur. Biophys. J.* **2007**, *36*, 239-252.

57. El Mkami, H.; Mohideen, M. I. H.; Pal, C.; McKinlay, A.; Scheimann, O.; Morris, R. E. EPR and magnetic studies of a novel copper metal organic framework (STAM-I). *Chem. Phys. Lett.* **2012**, *544*, 17-21.
58. Barnett, S. M.; Goldberg, K. I.; Mayer, J. M. A soluble copper–bipyridine water-oxidation electrocatalyst. *Nat. Chem.* **2012**, *4*, 498.
59. Godlewska, S.; Jezierska, J.; Baranowska, K.; Augustin, E.; Dołęga, A. Copper(II) complexes with substituted imidazole and chlorido ligands: X-ray, UV–Vis, magnetic and EPR studies and chemotherapeutic potential. *Polyhedron* **2013**, *65*, 288-297.
60. Peisach, J.; Blumberg, W. E. Structural implications derived from the analysis of electron paramagnetic resonance spectra of natural and artificial copper proteins. *Arch. Biochem. Biophys.* **1974**, *165*, 691-708.
61. Silva, K. I.; Michael, B. C.; Geib, S. J.; Saxena, S. ESEEM analysis of multi-histidine cu(ii)-coordination in model complexes, peptides, and amyloid-β. *J. Phys. Chem. B* **2014**, *118*, 8935-8944.
62. Tran, C. D.; Makuvaza, J.; Munson, E.; Bennett, B. Biocompatible Copper Oxide Nanoparticle Composites from Cellulose and Chitosan: Facile Synthesis, Unique Structure, and Antimicrobial Activity. *ACS Appl. Mater. Interfaces* **2017**, *9*, 42503-42515.
63. Xu, B.; Mei, Y.; Xiao, Z.; Kang, Z.; Wang, R.; Sun, D. Monitoring thermally induced structural deformation and framework decomposition of ZIF-8 through in situ temperature dependent measurements. *Phys. Chem. Chem. Phys.* **2017**, *19*, 27178-27183.
64. Li, G.; Kobayashi, H.; Kusada, K.; Taylor, J. M.; Kubota, Y.; Kato, K.; Takata, M.; Yamamoto, T.; Matsumura, S.; Kitagawa, H. An ordered bcc CuPd nanoalloy synthesised via the thermal decomposition of Pd nanoparticles covered with a metal-organic framework under hydrogen gas. *Chem. Commun.* **2014**, *50*, 13750-13753.
65. Lin, K.-S.; Adhikari, A. K.; Ku, C.-N.; Chiang, C.-L.; Kuo, H. Synthesis and characterization of porous HKUST-1 metal organic frameworks for hydrogen storage. *Int. J. Hydrogen Energy* **2012**, *37*, 13865-13871.
66. Topnani, N.; Kushwaha, S.; Athar, T. Wet synthesis of copper oxide nanopowder. *Int. J. Green Nanotechnol.* **2010**, *1*, M67-M73.
67. Chen, L.; Zhang, Y.; Zhu, P.; Zhou, F.; Zeng, W.; Lu, D. D.; Sun, R.; Wong, C. Copper salts mediated morphological transformation of Cu2O from cubes to hierarchical flower-like or microspheres and their supercapacitors performances. *Sci. Rep.* **2015**, *5*, 9672.
68. Zoroddu, M. A.; Medici, S.; Peana, M. Copper and nickel binding in multi-histidinic peptide fragments. *J. Inorg. Biochem.* **2009**, *103*, 1214-1220.
69. Shahmiri, M.; Ibrahim, N. A.; Shayesteh, F.; Asim, N.; Motallebi, N. Preparation of PVP-coated copper oxide nanosheets as antibacterial and antifungal agents. *J. Mater. Res.* **2013**, *28*, 3109-3118.
70. del Pino, P.; Yang, F.; Pelaz, B.; Zhang, Q.; Kantner, K.; Hartmann, R.; Martinez de Baroja, N.; Gallego, M.; Moller, M.; Manshian, B. B.; Soenen, S. J.; Riedel, R.; Hampp, N.; Parak, W. J. Basic physicochemical properties of polyethylene glycol coated gold nanoparticles that determine their interaction with cells. *Angew. Chem. Int. Ed.* **2016**, *55*, 5483-5487.
71. Kurtan, U.; Amir, M.; Yıldız, A.; Baykal, A. Synthesis of magnetically recyclable MnFe2O4@SiO2@Ag nanocatalyst: Its high catalytic performances for azo dyes and nitro compounds reduction. *Appl. Surf. Sci.* **2016**, *376*, 16-25.
72. Cui, X.; Zheng, Y.; Tian, M.; Dong, Z. Novel yolk–shell-structured Fe3O4@γ-AlOOH nanocomposite modified with Pd nanoparticles as a recyclable catalyst with excellent catalytic activity. *Appl. Surf. Sci.* **2017**, *416*, 103-111.